Fei Ma*, Shengbo Wang, Yanfei Guo, Cuixia Dai and Jing Meng*

Image segmentation of mouse eye *in vivo* with optical coherence tomography based on Bayesian classification

Abstract

Objectives: Optical coherence tomography (OCT) is a new imaging technology that uses an optical analog of ultrasound imaging for biological tissues. Image segmentation plays an important role in dealing with quantitative analysis of medical images.
Methods: We have proposed a novel framework to deal with the low intensity problem, based on the labeled patches and Bayesian classification (**LPBC**) model. The proposed method includes training and testing phases. During the training phase, firstly, we manually select the sub-images of background and Region of Interest (ROI) from the training image, and then extract features by patches. Finally, we train the Bayesian model with the features. The segmentation threshold of each patch is computed by the learned Bayesian model.
Results: In addition, we have collected a new dataset of mouse eyes *in vivo* with OCT, named **MEVOCT**, which can be found at URL https://17861318579.github.io/LPBC. MEVOCT consists of 20 high-resolution images. The resolution of every image is 2048 × 2048 pixels.
Conclusions: The experimental results demonstrate the effectiveness of the LPBC method on the new MEVOCT dataset. The ROI segmentation is of great importance for the distortion correction.

Keywords: mouse eye *in vivo*; optical coherence tomography; image segmentation; labeled patches

*Corresponding authors: Fei Ma and Jing Meng**, School of Computer Science, Qufu Normal University, Yantai Road, Rizhao, 276827, Shandong, China, E-mail: mafei0603@163.com (F. Ma), jingmeng@qfnu.edu.cn (J. Meng). https://orcid.org/0000-0002-5472-4763 (F. Ma)
Shengbo Wang and Yanfei Guo, School of Computer Science, Qufu Normal University, Rizhao, Shandong, China, E-mail: 17861318579@163.com (S. Wang), guo_1992_fei@163.com (Y. Guo)
Cuixia Dai, Department of College Science, Shanghai Institute of Technology, Shanghai, Shanghai, China, E-mail: Sdadai7412@163.com

Introduction

Digital medical image processing has gradually become a hot topic. In recent years, countless researchers have mainly focused on the quantitative analysis of optical coherence tomography (OCT) images [1–3], which includes biomedical image denoising, image reconstruction, and disease recognition [4, 5]. However, conventional measurements are based on OCT images, which suffer from distortion due to various mechanisms. Due to the refraction of the probe light in the sample and the scan geometries, there are distortions in the OCT images. To improve the accuracy of the curvature, the distortion correction for OCT images is a serious requirement [6, 7] in Figure 1(a) and (b). This will need to locate the edges and region of the organs. Segmentation is one of the fundamental technologies for analyzing retinal images *in vivo* by OCT [8, 9]. The ROIs of medical images can be identified by segmentation, which can be useful for image analysis and image understanding.

Recently, OCT has been widely used to image the eye *in vivo*. There are many types of eye diseases [10–13], such as multiple sclerosis (MS), diabetic retinopathy (DR), glaucoma and age-related macular degeneration (AMD). However, there are distortions in the retinal images due to the fan-shaped scanning pattern. The distortion of the fundus image can be corrected according to the geometric coordinate relationship between the OCT data matrix and the angular scanning mode [14, 15]. It needs the edges and locations of the retinal tissues to correct the distortion. Therefore, there is a serious demand for automatic segmentation algorithms without human interaction, as shown in Figure 1(a) and (b). However, there are many drawbacks to medical image segmentation, such as a. Collecting and labeling the dataset requires trained experts in the relevant fields [4, 16, 17]. This is a valuable and expensive task that requires a lot of effort. In this work, we collect a new dataset on mouse eyes *in vivo* with OCT, which will be helpful for further research.

As mentioned above, these methods focus on segmentation under normal illumination and have achieved better performance in image segmentation to some extent. However, the images have some limitations, such as low intensity and low contrast. Figure 1(c) and (d) show the pixel distribution of ROIs and background. We extract many features by labeling
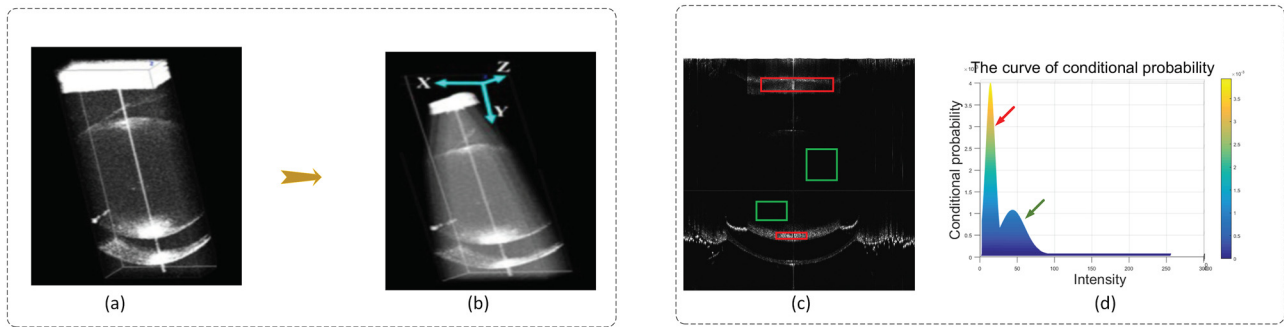
Figure 1: The typical application scenario and the pixels distribution of mouse eye *in vivo* by OCT. (a) and (b) Is one of the typical application scenario. Correction of refractive distortion is used in whole-eye optical coherence tomography imaging of the mouse eye. (c) The original image by OCT; (d) the Gaussian distribution of pixels.

patches from the original images. The pixels are extracted from ROI (in the red rectangle) and background (in the green rectangle) respectively in Figure 1(c). The left curve with the red arrow represents the pixels from the background and the right curve with the green arrow represents the pixels from the ROI in Figure 1(d). It can be seen that the pixel distribution basically follows the Gaussian distribution. Motivated by the above analysis, we intend to solve the few-shot and low-intensity problem based on the labeled patches and Bayesian classification.

The main contributions of our work are as follows.

(1) We designed a framework to address the low-intensity problem, called labeled patches and Bayesian-based classification (LPBC), for image segmentation of mouse eyes *in vivo* by OCT.

(2) We collected a new dataset of mouse eye *in vivo* by OCT, which will be valuable for the wide research. The data set contains 20 images. The size of the images is 2048×2048 pixels. The intensity of each image is low.

(3) We conducted extensive experiments on the new OCT mouse eye dataset. Our method obtained the accurate edge structure of the ROIs and achieved competitive overall performance.

The rest of this paper is structured as follows: Section "Related work" describes work related to image segmentation. Section "Methods" presents the details of the proposed approach, and Section "Data set and experiments" shows the experimental results. Section "Discussion" gives the discussion on LPBC. Conclusions concludes the paper and discusses future work.

Related work

The image segmentation methods mainly include two categories: the traditional statistics-based models [18–20] and the

deep learning methods [21–23]. The threshold segmentation algorithm is widely used for image segmentation. The basic idea is to obtain the threshold value from local areas or global images based on the statistics or learning algorithm. OTSU [24, 25] and MinError [26, 27] are the typical statistical algorithms for the global threshold. Malathi et al. [28] integrated OTSU and active contour segmentation to separate lung nodules from chest CT images. Recently, the learning based thresholding methods [29, 30] can obtain the adaptive threshold for the whole image, which can achieve better performance in image segmentation.

In recent years, deep-learning methods have been applied to medical imaging field [31–34]. In addition, the convolutional neural network (CNN)-based methods [35–37] have been proposed to learn the effective features from training samples for better image segmentation. In 2015, Ronneberger presented U-Net [38], which is an effective convolutional neural network for biomedical image segmentation. U-Net is based on fully convolutional networks for biomedical image segmentation. The network architecture of U-Net consists of a contraction path (encoder) and an expansion path (decoder). The number of feature channels is doubled in the encoder stage. The feature map is upsampled by upconvolution in the decoder stage. Subsequently, many methods based on U-Net are presented to segment the biomedical images [39–41]. Some researchers [42–44] have integrated ResNet and U-Net for image segmentation. Deep residual networks (ResNet) [45, 46] involved the insertion of shortcut connections to transform a simple network into its residual network counterpart. However, there are few deep learning methods for whole-eye segmentation of the mouse in OCT images.

Methods

In this section, we elaborate on the proposed labeled patches and Bayesian classification-based segmentation (LPBC) approach. An
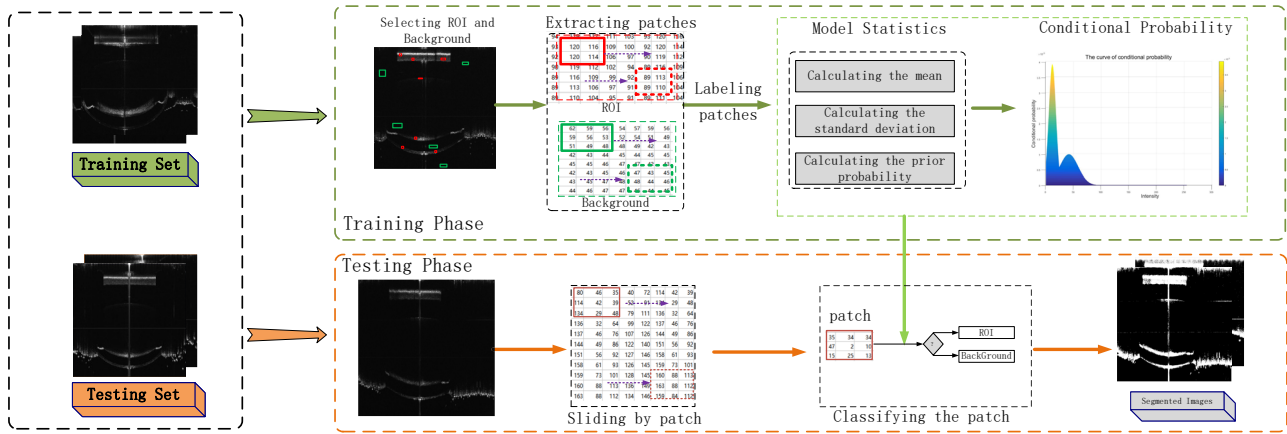
Figure 2: The flowchart of labeled patches and Bayesian based classification (LPBC). The original dataset is divided into two subsets, i.e., the training set and testing set. In the training phase, feature vectors are extracted by patches (taking 3×3 pixels as an example). The Gaussian Naive Bayesian model is trained by patches with labels 1 or 2. In the testing phase, the feature vectors of testing images are extracted by sliding the patch. Finally, the binarized images are obtained with the trained model. The dotted lines represent sliding forward.

overview of LPBC on mouse eyes is shown in Figure 2. It contains two stages: in the training stage, firstly, we manually select the background (in green box) and ROI (in red box) from the training images respectively. Then, we extract the features from the ROI and background by patch. Finally, the Bayesian classifier model is trained with the features. In the testing stage, features are extracted from the images by patch in the testing set, then the segmentation thresholding value of every patch is computed by the trained Bayesian model. Finally, the binarized image is obtained with the trained model. The main advantages of our proposed method have two folds: (1) As the above analysis, the pixels of ROIs and background follow the Gaussian distribution. LPBC integrates the ideas of the Bayesian classifier and Gaussian distribution. (2) Our model can extract plenty of features from each image by patch, which is favorable for a few-shot problem. These steps are described in detail in the following sections. These steps are described in detail in following sections.

Feature extraction

In this work, we directly extract the features from the image by patch. Firstly, the entire data set is divided into the training set and testing set. We select 3 samples for training randomly since the number of samples by OCT is limited. The remainder of data is the testing set. Secondly, we select several sub-images as the ROI and background from every training sample manually. Note that the sizes of sub-images are bigger than $d \times d$ pixels, d is the size of the labeling patch (taking 3×3 [d=3] pixels as an example in Figure 2). Finally, features are extracted by patches from each sub-image and labeled as 1 (as ROI) or 2 (as background). In experiments, we set the size of the patch to 8×8. Figure 2 shows the process of extracting features by patch. For the test samples, features are extracted by moving the whole image with the patch 8×8.

Gaussian Naive Bayes classification

The Naive Bayes classification is a probabilistic classification algorithm based on Bayes theorem [47], which belongs to supervised learning. It has been widely used for many classifications [48, 49] and incorporates

strong independence assumptions, i.e., the features are assumed to be independent. As shown in Figure 1, the pixels of the patch follow the Gaussian distribution. Therefore, in this work, we utilize the Gaussian Naive Bayes Classification to binarize the images of mouse eyes *in vivo* with OCT.

Suppose $X = \{X_1, X_2, \dots, X_n\}$, $X \subseteq R^n$ as the patch set of mouse eye images. n is the patch number of training samples. The training set is $T = \{(X_1, y_1), \dots (X_i, y_i), \dots (X_n, y_n)\}$, where y_i is the label of the *ith* patch X_i. y_i is the *ith* class, where $i \in \{1, 2\}$. $X_i = \{x_i^1, x_i^2, \dots, x_i^d\}$ is one feature vector, where d is the feature vector dimension of every patch.

Then, the Bayes' theorem is defined as

$$p(Y = C_k \mid X_i) = \frac{p(X_i \mid Y = C_k) p(Y = C_k)}{\sum_{j=1}^{K} p(X_i \mid Y = C_j) p(Y = C_j)}, \tag{1}$$

where C_k is the number of classes, $C_k=\{1, 2\}$. The prior probability $p(Y=C_k)$ is calculated as follows:

$$p(Y = C_k) = \frac{n_{(Y=C_k)}}{n}, \tag{2}$$

where $n_{(Y=C_k)}$ represents the number of samples corresponding class. As the above analysis, the likelihood of the features of every patch is assumed to be Gaussian, hence, we assume that any two events are independent, then, conditional probability can be given as follows:

$$p(X_i \mid Y) = \prod_{j=1}^{d} \frac{1}{\sqrt{2\pi\sigma_{(j,Y)}^2}} \exp\left(-\frac{(x_i^j - \mu_{(j,Y)})^2}{2\sigma_{(j,Y)}^2}\right), \tag{3}$$

where $\mu_{(j,Y)}$ denotes the mean of each attribute x^j corresponding class $(Y=C_k)$. $\sigma_{(j,Y)}$ means the standard deviation of each attribute x^j corresponding class $(Y=C_k)$.

Finally, we can calculate the probability of the given set of inputs for all possible values of the class and get the output with maximum probability. This can be expressed mathematically as:

$$y = f(X_i) = \underset{Y}{\operatorname{argmax}}\left\{p(Y = C_k) \prod_{j=1}^{d} p(x_j \mid Y = C_k)\right\}. \tag{4}$$

The segmentation based on the labeled patches and Gaussian Naive Bayes is summarized as Algorithm 1.

Algorithm 1. Labeled patches and Gaussian Naive Bayes classification for segmentation.

Input: The images of mouse eye *in vivo* by OCT
Output: The segmented images
1: Preparation: Partitioning the training set and testing set.
2: Training phase:
3: Step 1: Extracting the feature vectors from images by patch and labeling every patch as ROI (background);
4: Step 2: Calculating the prior probability p($Y=C_k$) by Eq. (2);
5: Step 3: Calculating the mean of each attribute x^j corresponding class ($Y=C_k$) and the standard deviation of each attribute x^j corresponding class ($Y=C_k$), respectively.
6: Testing phase:
7: Step 1: Extracting feature from testing image by sliding the patch;
8: Step 2: Computing the conditional probability of the current patch by Eq. (3);
9: Step 3: Calculating the posterior probability of the patch by Eq. (4);
10: Step 4: Obtaining the maximum posterior probability among all classes;
11: Step 5: The segmented image is obtained.

Data set and experiments

We collect a new dataset of **m**ice **e**ye *in vivo* with **OCT**, named as **MEVOCT**.[1] To evaluate the effectiveness of our approach, we conduct extensive experiments on the new dataset MEVOCT.

Datasets and settings

Dataset

In this section we briefly summarize the new MEVOCT dataset collected by the customized swept source optical coherence tomography (SS-OCT) system. Figure 3 shows the collection of MEVOCT. The mouse is then placed in the box. If its eyes are directed towards the probe of the infrared refractometer, the light can enter the mouse's eyes. Finally, we can get the images of the mouse eye *in vivo* with the SS-OCT system.

In the experiments, we generate the data set with our OCT system. We use a custom-built spectral domain OCT (SD-OCT) system to obtain three-dimensional images of mouse eyes by telecentric scanning. The lateral resolution of the SD-OCT system is approximately 15.9 μm. The axial resolution is approximately 6.4 μm. The imaging system uses a super light emitting diode (SLED, inphonix, USA) as the light source laser to provide an imaging rate of 30 kHz. In

---

1 MEVOCT dataset and MakeGT for Ground truth can be found at URL: https://17861318579.github.io/LPBC.

experiments, the central wavelength is 840 nm, the bandwidth is 100 nm, and the imaging object is illuminated with a maximum imaging depth of 5.7 mm. Each B-scan consists of 1024 A-scans and 256 B-scan position scans to create a three-dimensional OCT image of the eye.

There are 20 images in total. The size of each image is 2048×2048 pixels with one channel. To handle the few-shot problem, we select 3 images as the training set and the rest images are the testing set by 10-fold cross-validation. Mouse eyes mainly contain four tissues: retina, lens, iris, and cornea. In our experiments, we mainly extract the regions of these tissues as ROIs. The areas in the red rectangle in Figure 4 are ROIs. The ground-truth sample is manually made by a trained expert and aided by our self-developed software **MakeGT_v1.0**. We process images with MATLAB and calculate the evaluation metrics with Python. In experiments, we select the patch size as 8×8 pixels (Figure 4).

Evaluation metrics

To evaluate the performances of the methods, the evaluation metrics are adopted as follows:

- Sensitivity is one of the most widely statistical measures, also known as the true positive rate, which counts the proportion of true positives that are correctly identified as ROIs. Sensitivity is computed by $\frac{TP}{TP+FN}$, where TP is the number of true positive pixels and FN is a false negative in ROIs.
- Specificity is selectivity or true negative rate (TNR), which measures the proportion of true negatives (i.e., pixels belong to the background) that are correctly identified as negatives. Specificity is obtained by $\frac{TN}{TN+FP}$.
- The dice coefficient can measure the number of positives pixels in ROIs while penalizing for the false positives in background areas. Dice coefficient is calculated by $\frac{2 \times TP}{FP+FN+2 \times TP}$, where TN is the number of true negative pixels, and FN is the number of false negative pixels. Accuracy is computed by $\frac{TN+TP}{FP+FN+TN+TP}$.

The Hausdorff distance (HD) [50] was used as a measure to compare binary images or portions thereof. The Hausdorff distance $HD(O_q, E_q)$ between O_q and E_q is given by $HD(O_q, E_q) = \max(hd(O_q, E_q), hd(E_q, O_q))$, where $hd(O_q, E_q) = \max_{o \in O_q} \min_{e \in E_q} \|o - e\|_2$ and $hd(E_q, O_q) = \max_{e \in E_q} \min_{o \in O_q} \|o - e\|_2$.

Compared methods

To evaluate the performance of our approach LPBC, we select several related methods as the compared methods, including
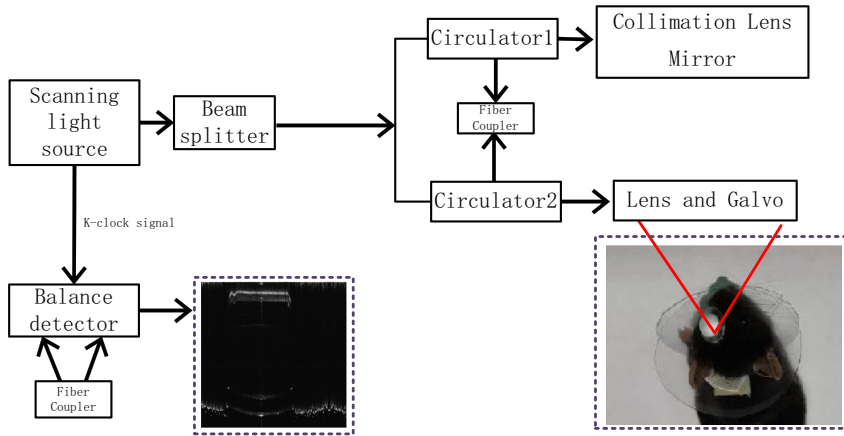
Figure 3: Illustration of swept source OCT (SS-OCT) pipeline. SS-OCT has been used in qualitative and quantitative analysis of the retina, vitreous, and optic disc. SS-OCT devices operate at speeds greater than 100 kHz. Therefore, SS-OCT offers potential advantages in visualization of the choroid and sclera. The right sub image is a mouse with collar.
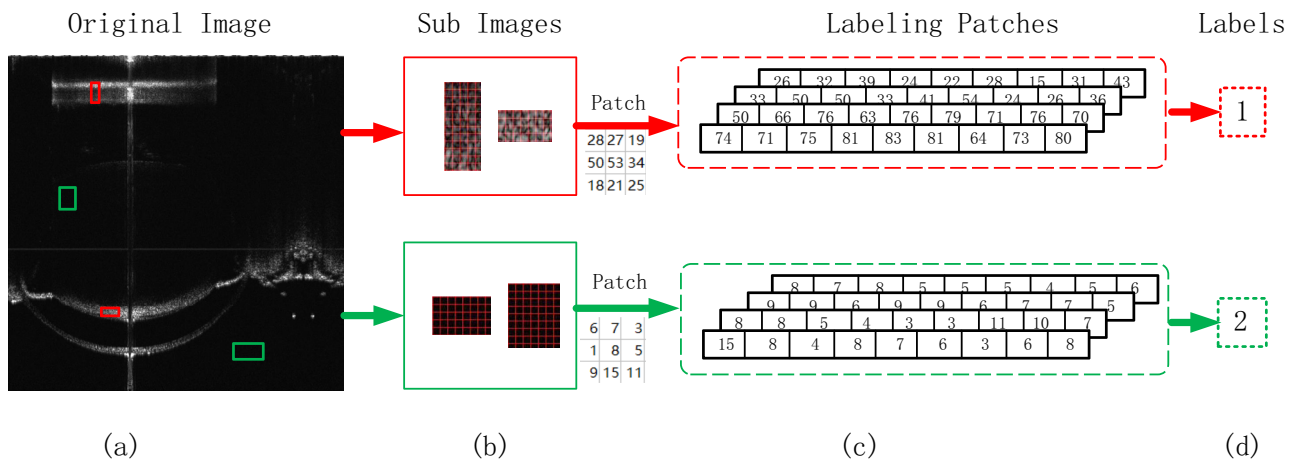

Figure 4: The flowchart of extracting feature and labeling patches. (a) The original image. The regions in red rectangle are ROIs while those in green rectangle are background. (b) The sub images are from the original image. The size of each patch is d × d pixels. Taking d=3 as an example. (c) The patch features are transferred into one-dimension vector. (d) The features of patches are labeled with 1 and 2 respectively.

OTSU [51, 52], Iteration [53], MinError [54], U-Net[2] [38] and Resnet34-U-Net [38]. In experiments, we perform competitive methods with the codes provided by the authors.

Evaluation on the MEVOCT dataset

Following the evaluation protocol in the literature [55], we perform experiments on the MEVOCT dataset for testing. Table 1 reports the results of LPBC and the competing methods on the new MEVOCT dataset. It can be observed that our LPBC performs better than the other competing methods.

In particular, our LPBC achieves 80.12 % (sensitivity), 94.12 % (specificity) and 65.16 % (cube coefficient). The traditional methods such as OTSU, iteration and MinError achieve lower performance than the deep learning methods. OTSU

2 https://github.com/Andy-zhujunwen/U-Net-ZOO.

achieves only 32.71 % sensitivity among all methods. The deep learning methods achieve better performance on the following metrics. U-Net achieves 68.19 % on sensitivity, 30.61 on Hausdorff distance (HD) and achieves the best performance on specificity, which means that U-Net can accurately detect more pixels of background than other methods.

LPBC achieves the best performance, i.e., 80.12 % in sensitivity, 65.16 % in dice coefficient and 96.33 % in accuracy,

Table 1: The results of different methods on the MEVOCT database. Best results are in bold.

Methods	Sensitivity	Specificity	DC	Acc	HD
Iteration	43.97 %	98.23 %	51.89 %	91.67 %	33.11
OTSU	32.41 %	98.84 %	43.55 %	91.26 %	31.95
MinError	34.65 %	98.65 %	42.39 %	92.90 %	32.63
U-Net	68.19 %	**99.39 %**	64.96 %	96.09 %	**30.61**
Resnet43-U-Net	65.21 %	98.42 %	64.69 %	95.91 %	31.12
LPBC (Ours)	**80.12 %**	94.12 %	**65.16 %**	**96.33 %**	30.63

which means that our approach can correctly detect the most pixels of ROIs in the images among all the methods. The results demonstrate the effectiveness of our proposed LPBC.

Figure 5 shows the visual comparison of all the methods. We select one of the test results from the test set to show the details. The top row is the original image and the results of the different methods. The bottom row is the details of the corresponding results in the red rectangle in the first row. From the details of the results, LPBC can get the best visual appearance. The results of the deep learning methods are poor, which may be due to the few-shot problem. Although the results of OTSU, Iteration and MinError are better, there are many FN pixels in the ROIs, i.e., the pixels of the ROIs are identified as background.

Effect on patch size

In this work, we use the labeled patches to extract the features from each image, which is favorable for the few-shot scene. The flowchart of the labeled patch extraction is shown in Figure 4. The patches belonging to ROI and background respectively are labelled with different labels. The patch sizes have an impact on the performance of the segmentation images. In this section, the patch sizes range from 3×3 (pixels) to 9×9 (pixels), while the other parameters are fixed.

Table 2 shows the results of different patch sizes on the MEVOCT dataset. We can see that the sensitivity is highest when the patch size is 8×8. The sensitivity reaches 65.81 %. When the patch size is 8×8 pixels, the specificity, accuracy and dice coefficient are the highest. HD gives the lowest result. Therefore, we choose the patch size of 8×8 pixels in this work.

Data augmentation

Augmentation methods can be used to increase the size of the training data for all methods, so we perform data

Table 2: The results of different patch sizes on the MEVOCT dataset. Best results are in bold.

Patch size	Sensitivity	Specificity	DC	Acc	HD
3×3	65.81 %	**95.56 %**	60.92 %	95.39 %	32.66
5×5	74.71 %	95.20 %	64.06 %	94.55 %	33.13
6×6	75.83 %	94.97 %	64.26 %	95.63 %	31.67
7×7	76.78 %	94.82 %	64.35 %	96.15 %	31.89
8×8	**80.12 %**	94.12 %	**65.16 %**	**96.33 %**	**30.63**
9×9	78.50 %	94.40 %	64.00 %	96.01 %	32.03

augmentation on our dataset, including 90° rotation, horizontal rotation, 270° rotation, vertical rotation, and blur operation. Therefore, each image in our dataset is expanded to 6 images. The training set was also expanded from 3 images to 18 images. We trained and tested the augmented dataset using our approach and two deep learning methods.

The sensitivity, specificity and dice coefficient of U-Net are 81.09 , 91.77 and 57.89 % respectively. The sensitivity, specificity and dice coefficient of Resnet34-U-net are 72.18 , 96.62 and 63.91 % respectively. The sensitivity, specificity, dice coefficient, Acc and HD of LPBC (Ours) are 82.14 , 93.70, 68.68, 96.33 % and 30.63, respectively. There are therefore improvements in the sensitivity of both U-Net and Resnet34-U-Net. Specifically, the performance of U-Net is improved by 12.9 %. However, the specificity and the dice coefficient are obviously reduced. Although the specificity of our approach is lower than that of the original dataset, the sensitivity and dice coefficient of our methods are significantly improved with data augmentation. One can see that three metrics of our approach are higher than the deep learning methods.

Discussion

With the development of image acquisition equipment and machine learning methods, automatic eye image segmentation

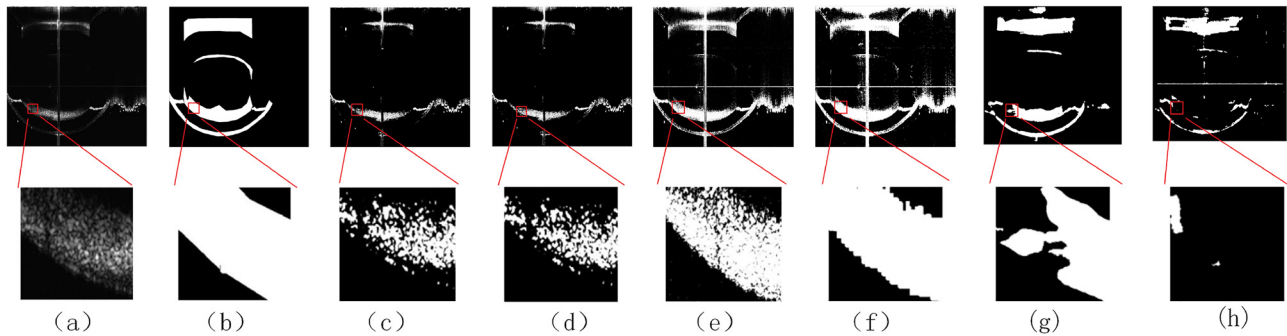(a)   (b)   (c)   (d)   (e)   (f)   (g)   (h)

Figure 5: Visual comparison of LPBC and other comparative methods. (a) The original image; (b) the ground-truth image. (c)–(h): The results by the OTSU, iteration, MinError, LPBC, U-Net and Resnet34-U-Net. One can see that the original image has many low-contrast areas.

has become a hot topic in the field of digital image processing. In this work, we design the labeled patch and Bayesian methods for image segmentation. On the one hand, the original resolution of the image is large. Plenty of patches can be extracted from the original samples. On the other hand, the number of original samples is small, so that the models for segmentation are insufficiently trained. Therefore, we consider manually selecting the ROI and the background in the original image. We extract the pixels by patches to improve the segmentation performance and train a more accurate segmentation model.

Bayesian segmentation method is considered as one of the thresholding methods in this paper. The mean of the pixels and the conditional probability of each patch have a significant effect on the segmentation. Therefore, we focus on the following: (1) The features of different eye tissues, such as iris, cornea, lens and retina, should be extracted before training the model. (2) We should extract the features from the different regions in the same tissues. (3) We should focus on the edge features. In addition, the selection on the patch size is optimized by the validation set.

In addition, there is an oversegmentation in the experimental results. On the one hand, we will acquire more samples with OCT for segmentation in the future. On the other hand, we will use new methods to extract useful features from the OCT samples.

Conclusions

In this paper, we proposed a labeled patch-based Gaussian Naive Bayes classification framework for image segmentation. Gaussian Naive Bayes classification was used as the backbone of the proposed framework. This framework consists of two main parts: labeled patches and Gaussian Naive Bayes model. We then compared the results with different models on the new MEVOCT dataset. The idea of labeled patches aims at extracting many patches from the few images, which is favorable for the few-shot scenes. Extensive experiments demonstrate the effectiveness of LPBC. Our approach can provide automatic segmentation of edges and tissue regions for distortion correction in OCT images.

The new MEVOCT dataset has been made publicly available, which will be useful for broad research. In addition, we will continue to expand and improve our dataset in the future.

References

1. Elsawy AS, Abdel-Mottaleb M. PIPE-Net: a pyramidal-input-parallel-encoding network for the segmentation of corneal layer interfaces in OCT images. Comput Biol Med 2022;147:105595.
2. Qin X, Wang B, Boegner D, Gaitan B, Zheng Y, Du X, et al. Indoor localization of hand-held OCT probe using visual odometry and real-time segmentation using deep learning. IEEE Trans Biomed Eng 2022; 69:1378–85.
3. Fu H, Xu Y, Lin S, Zhang X, Wong D, Liu J, et al. Segmentation and quantification for angle-closure glaucoma assessment in anterior segment OCT. IEEE Trans Med Imaging 2017;36:1930–8.
4. Viedma GA, Alonso-Caneiro D, Read SA, Collins MJ. OCT retinal and choroidal layer instance segmentation using mask R-CNN. Sensors 2016;22:2022.
5. Chong DY, Kim HJ, Lo P, Young S, McNitt-Gray MF, Abtin F, et al. Robustness-driven feature selection in classification of fibrotic interstitial lung disease patterns in computed tomography using 3D texture features. IEEE Trans Med Imaging 2016;35:144–57.
6. Tang N, Fan J, Zhang Y, Shi G. Correction of refractive and scattered image distortions in optical coherence tomography based on scalpel. J Phys Conf 2021;2024:012021–8.
7. Tan J, Qiu R, Ding X, Dai C, Meng J, Zhao J, et al. Correction of refractive distortion in whole-eye optical coherence tomography imaging of the mouse eye. J Biophotonics 2022;15:1–15.
8. Wang M, Zhu W, Shi F, Su J, Chen H, Yu K, et al. MsTGANet: automatic drusen segmentation from retinal OCT images. IEEE Trans Med Imaging 2022;41:394–406.
9. Bandyopadhyay T, Kubícek J, Penhaker M, Timkovic J, Oczka D, Krejcar O. A semi-supervised learning approach for automatic segmentation of retinal lesions using SURF blob detector and locally adaptive segmentation. In: ACIIDS, vol 2; 2019:311–23 pp.

10. Chen Z, Wang X, Huang J, Lu J, Zheng J. Deep attention and graphical neural network for multiple sclerosis lesion segmentation from MR imaging sequences. IEEE J Biomed Health Inf 2022;26:1196–207.

11. Ghribi O, Sellami L, Slima M, Hamida A, Mhiri C, Mahfoudh K. An advanced MRI multi-modalities segmentation methodology dedicated to multiple sclerosis lesions exploration and differentiation. IEEE Trans NanoBiosci 2017;8:656–65.

12. Li X, Hu X, Yu L, Zhu L, Fu C, Heng P. CANet: cross-disease attention network for joint diabetic retinopathy and diabetic macular edema grading. IEEE Trans Med Imaging 2020;5:1483–93.

13. Lin C, Liao W, Liang J, Chen P, Ko C, Yang C, et al. Denoising performance evaluation of automated age-related macular degeneration detection on optical coherence tomography images. IEEE Sensor J 2021;1:790–801.

14. Dai CX, Zhou CQ, Fan SH, Chen Z, Chai XY, Ren QS, et al. Optical coherence tomography for whole eye segment imaging. Opt Express 2012;20:6109–15.

15. Grytz R, El Hamdaoui M, Fuchs PA, Fazio MA, McNabb RP, Kuo AN, et al. Nonlinear distortion correction for posterior eye segment optical coherence tomography with application to tree shrews. Biomed Opt Express 2022;2:1070–86.

16. Mithun N, Panda R, Roy-Chowdhury AK. Construction of diverse image datasets from web collections with limited labeling. IEEE Trans Circuits Syst Video Technol 2020;30:1147–61.

17. Yao Y, Zhang J, Shen F, Liu L, Zhu F, Zhang D, et al. Towards automatic construction of diverse, high-quality image datasets. IEEE Trans Knowl Data Eng 2020;32:1199–211.

18. Bhandari A, Ghosh A, Kumar I. A local contrast fusion based 3D Otsu algorithm for multilevel image segmentation. IEEE/CAA J Autom Sin 2020;1:200–13.

19. Pang S, Lu Z, Jiang J, Zhao L, Lin L, Li X, et al. Hippocampus segmentation based on iterative local linear mapping with representative and local structure-preserved feature embedding. IEEE Trans Med Imaging 2019;10:2271–80.

20. Mohsen G, Vahid A. Unsupervised change detection in polarimetric SAR data with the hotelling-lawley trace statistic and minimum-error thresholding. IEEE J Sel Top Appl Earth Obs Remote Sens 2018;12:4551–62.

21. Zhang T, Yang Z, Xu Z, Li J. Wheat yellow rust severity detection by efficient DF-UNet and UAV multispectral imagery. IEEE Sensor J 2022;9:9057–68.

22. Wang M, Jiang H, Shi T, Yao Y. HD-RDS-UNet: leveraging spatial-temporal correlation between the decoder feature maps for lymphoma segmentation. IEEE J Biomed Health Inf 2022;3:1116–27.

23. Zhang Y, Wu J, Liu Y, Chen Y, Wu E, Tang X. MI-UNet: multi-inputs UNet incorporating brain parcellation for stroke lesion segmentation from T1-weighted magnetic resonance images. IEEE J Biomed Health Inf 2021;2:526–35.

24. Chen C, Wang X, Heidari AA, Yu H, Chen H. Multi-threshold image segmentation of maize diseases based on elite comprehensive particle swarm optimization and Otsu. Front Plant Sci 2021;1:789911.

25. Yu Y, Bao Y, Wang J, Chu H, Zhao N, He Y, et al. Crop row segmentation and detection in paddy fields based on treble-classification Otsu and double-dimensional clustering method. Remote Sens 2021;5:901–13.

26. Tao P, Wei C, Yi H, Lou Y, Ying Z. A method based on minimum error thresholding for froth image classification. In: 25th Chinese control and decision conference (CCDC), vol 1; 2013:4768–71 pp.

27. Sayed MS. Robust fabric defect detection algorithm using entropy filtering and minimum error thresholding. In: IEEE 59th international midwest symposium on circuits and systems (MWSCAS), vol 1; 2016:1–4 pp.

28. Malathi M, Kalaiselvi K, Shankarlal B, Kokila S, Thenmalar K, Johny R. A hybrid deep learning model for effective segmentation and classification of lung nodules from CT images. J Intell 2022;3:2667–79.

29. Kang S, Iwana B, Uchida S. Cascading modular U-nets for document image segmentation. In: International conference on document analysis and recognition (ICDAR), vol 1; 2019:118–30 pp.

30. Yang X, Wan Y. Non-uniform illumination document image segmentation using K-means clustering algorithm. In: IEEE 9th international conference on information, communication and networks (ICICN), vol 1; 2021:506–10 pp.

31. Roy S, Menapace W, Oei S, Luijten B, Fini E, Saltori C, et al. Deep learning for classification and localization of COVID-19 markers in point-of-care lung ultrasound. IEEE Trans Med Imaging 2020;8:2676–87.

32. Kromp F, Fischer L, Bozsaky E, Ambros IM, Dörr W, Beiske K, et al. Evaluation of deep learning architectures for complex immunofluorescence nuclear image segmentation. IEEE Trans Med Imaging 2021;1:1934–49.

33. Hussein S, Kandel P, Bolan CW, Wallace MB, Bagci U. Lung and pancreatic tumor characterization in the deep learning era: novel supervised and unsupervised learning approaches. IEEE Trans Med Imaging 2019;38:1777–87.

34. Ma D, Lu DH, Chen S, Heisler M, Dabiri S, Lee S, et al. LF-UNet – a novel anatomical-aware dual-branch cascaded deep neural network for segmentation of retinal layers and fluid from optical coherence tomography images. CMIG (Comput Med Imaging Graph) 2021;94:101988–97.

35. Swalpa K, Gopal K, Shiv R, Bidyut B. HybridSN: exploring 3-D-2-D CNN feature hierarchy for hyperspectral image classification. IEEE Geosci Remote Sens Lett 2020;17:277–81.

36. Cheng G, Yan B, Shi P, Li K, Yao X, Guo L, et al. Prototype-CNN for few-shot object detection in remote sensing images. IEEE Trans Geosci Rem Sens 2022;60:1–10.

37. Tan J, Gao Y, Liang Z, Cao W, Marc J, Huo Y, et al. 3D-GLCM CNN: a 3-dimensional gray-level co-occurrence matrix-based CNN model for polyp classification via CT colonography. IEEE Trans Med Imaging 2020;39:2013–24.

38. Ronneberger O, Fischer P, Brox T. U-net: convolutional networks for biomedical image segmentation. In: MICCAI, vol 1; 2015:234–41 pp.

39. Mai Y, Chen Z, Yu B, Li Y, Pang Z, Han Z. Non-contact heartbeat detection based on ballistocardiogram using UNet and bidirectional long short-term memory. IEEE J Biomed Health Inf 2022;26:3720–30.

40. Steven G, Amir A, Siddhartha S, Parag V. Fully dense UNet for 2-D sparse photoacoustic tomography artifact removal. IEEE J Biomed Health Inf 2020;24:568–76.

41. Song A, Xu L, Wang L, Yang X, Xu B, Wang B, et al. Automatic coronary artery segmentation of CCTA images with an efficient feature-fusion-and-rectification 3D-UNet. IEEE J Biomed Health Inf 2022;26:1–7.

42. Ali K, Ali A, Bagher R. ISUR: iris segmentation based on UNet and ResNet. In: 2021 11th international conference on computer engineering and knowledge (ICCKE); 2021:1–7 pp.

43. Abdul Q, Abdesslam B, Moona M, Mohamed A-N, Domenec P. Automatic segmentation of head and neck (H N) primary tumors in PET and CT images using 3D-inception-ResNet model. In: HECKTOR@MICCAI; 2021:58–67 pp.

44. Aheli S, Yu-Dong Z, Suresh C. Brain tumour segmentation with a muti-pathway ResNet based UNet. J Grid Comput 2021;19:43–53.

45. Xiao X, Lian S, Luo Z, Li S. Weighted res-unet for high-quality retina vessel segmentation. In: ITME, vol 1; 2018:327–31 pp.

46. Zhang Z, Liu Q, Wang Y. Road extraction by deep residual UNet. IEEE Geosci Remote Sens Lett 2018;15:749–53.

47. Berrar D. Bayes' theorem and naive Bayes classifier encycl. Bioinf Comput Biol 2018;1:403–12.

48. Mansour EA, Saleh AI, Mohammed Badawy M, Ali HA. Accurate detection of covid-19 patients based on feature correlated naïve Bayes (FCNB) classification strategy. J Ambient Intell Hum Comput 2022;13: 41–73.

49. Xiong Y, Ye M, Wu C. Cancer classification with a cost-sensitive naive Bayes stacking ensemble. Comput Math Methods Med 2021;1:1–12.

50. Karimi D, Salcudean SE. Reducing the Hausdorff distance in medical image segmentation with convolutional neural networks. IEEE Trans Med Imaging 2020;39:499–513.

51. Otsu N. A threshold selection method from gray-level histograms. IEEE Trans Syst Man Cybern 1979;9:62–6.

52. Xing JG, Yang P, Qing L. Robust 2D Otsu's algorithm for uneven illumination image segmentation. Comput Intell Neurosci 2020; 5047976:1–14.

53. Shaikh SH, Maiti AK, Chaki N. Image segmentation using iterative partitioning: a global thresholding approach. In: ReTIS, vol 1; 2011: 281–6 pp.

54. Barron OT. A generalization of Otsu's method and minimum error thresholding. In: ECCV, vol 5; 2020:455–70 pp.

55. Jadon S. A survey of loss functions for semantic segmentation. In: IEEE international conference on computational intelligence in bioinformatics and computational biology, vol 1; 2020:1–7 pp.